# Controlled electrodeposition of gold on graphene

Ananthoj, Balakrishna; Biroju, Ravi K.; Theis, Wolfgang; Dryfe, Robert A. W.

*DOI:*
10.1002/smll.201901555

# Controlled Electrodeposition of Gold on Graphene: Maximisation of the Defect-Enhanced Raman Scattering Response

Balakrishna Ananthoju[1, *], Ravi K. Biroju[2], Wolfgang Theis[2], Robert A. W. Dryfe[1, *]

[1]School of Chemistry and National Graphene Institute, University of Manchester,

Oxford Road, Manchester M13 9PL, UK

[2]Nanoscale Physics Research Laboratory, School of Physics and Astronomy,

University of Birmingham B15 2TT, UK

*Corresponding authors: balakrishna.ananthoju@manchester.ac.uk (Dr. Balakrishna Ananthoju)

robert.dryfe@manchester.ac.uk (Prof. Robert A. W. Dryfe)

**Keywords:** Graphene; Plasma, Defects, Raman spectroscopy.

**Abstract:**

A reliable method to prepare a surface-enhanced Raman scattering (SERS) active substrate is developed herein, by electrodeposition of gold nanoparticles (Au NPs) on defect-engineered, large area CVD graphene (GR). A plasma treatment strategy has been used in order to engineer the structural defects on the basal plane of large area single-layer graphene. This defect-engineered Au functionalised GR, offers reproducible SERS signals over the large area GR surface. The Raman data, along with X-ray photoelectron spectroscopy and analysis of the water contact angle are used to rationalise the functionalization of the graphene layer. We find that Au NPs functionalisation of the "defect-engineered" graphene substrates permits detection of concentrations as low as $10^{-16}$ M for the probe molecule Rhodamine B (RhB), which offers an outstanding molecular sensing ability. Interestingly, a Raman signal enhancement of up to$\sim 10^{8}$ was achieved. Moreover, we observed that GR effectively quenches the fluorescence background from the Au NPs and molecules due to the strong resonance energy transfer between Au NPs and GR. The results presented offer significant direction for the design and fabrication of ultra-sensitive SERS platforms, and also open up

possibilities for novel applications of defect engineered graphene in biosensors, catalysis, and optoelectronic devices.

## 1. Introduction

Surface-enhanced Raman spectroscopy (SERS) has been widely used for the analysis of ultra-low concentrations of molecules of biochemical and other analytical significance [1-3]. Among various traditional molecular detection approaches, SERS is a non-destructive and surface-sensitive technique allowing single molecule level detection with high sensitivity and selectivity [4-6]. Moreover, the SERS signals can be amplified by a factor of $10^{12}$–$10^{15}$ through highly localized surface plasmonic (LSP) oscillations, enabling the possibility of single molecule detection [7]. Two major theories, specifically those describing chemical (CEM) and electromagnetic (EM) enhancement, are widely invoked to explain the enhancement mechanisms, although the exact enhancement mechanism is still a matter of debate in the literature [8]. CEM relies on the charge transfer between chemisorbed species and the metal surface [8]. EM provides the leading contribution (typically by a factor of $10^8$) for the SERS enhancement, which generally originates from the magnification of the electric field by the excitation of LSPs of the underlying SERS active material [9]. One of the strategies is to improve the EM enhancement further by increasing the coupling with the LSPs. Theory predicts that the LSP coupling strongly depends on the separation distance between the nanoparticles (NPs), which have been confirmed experimentally. Thus, controlling the distance is a promising avenue to improve the SERS enhancement factor [9, 10]. It has been observed that the EM enhancement can be drastically increased with the decrease of the separation distance between NPs [9, 10]. Therefore, controlling the separation distance to sub-nanometre scales precisely is a promising approach to further improve the enhancement factor of the SERS. In this respect, incorporation of defect-engineered graphene along with gold can enhance the light absorption by the localized surface plasmon resonance (LSPR). Among various 2D materials, graphene has been proven to be an excellent substrate for the SERS towards the detection of the molecules due to its tuneable plasmon frequencies in the infrared and

terahertz frequencies [11-13]. This is attributed to the low optical absorption of graphene and its plasmon lying in the THz frequency range, i.e. very far from the visible range. It has been stated that SERS with graphene, also known as graphene-enhanced Raman spectroscopy (GERS), is only due to the CEM and not the EM contribution [14-16]. So far, graphene has been used in various sensing applications only for functionalization of metallic surfaces which support surface plasmon polaritons (SPPs) [17]. In recent times, it has been shown that graphene can support both SPPs and LSPs in mid- and far-infrared frequencies[18-20]. Additionally, it has been demonstrated that graphene can also effectively quench the spectral fluorescence background of the molecules [21, 22]. These facts can be effectively used for making highly efficient LSPR sensors. Therefore, graphene along with coupling of LSPs can be used to improve the sensitivity of the SERS.

For practical applications such as sensing, particularly single molecule detection, it is essential to tune the EM enhancement to obtain higher SERS enhancement factors. Some experiments have shown that the SERS activity can be tuned by modifying the graphene surface, i.e. by exploiting p and n-type doping to improve the sensitivity or UV/ozone oxidation treatment to improve the detection sensitivity [23, 24]. It has been observed that the near-field plasmonic effects can effectively tune the EM enhancement [11]. This can be achieved by controlling the metal NPs size and the periodicity of the NPs [11]. For example, Ferrari *et al.* have investigated the effect of Au NPs size and periodicity of the NPs on the graphene and they concluded that the SERS is due to the EM enhancement [11]. They used lithographic technique to control the periodicity of the NPs. However, there are practical limitations to control the NPs periodicity to sub-nanometer scales using lithography. There are no reports so far based on the defect engineered graphene with gold as a SERS substrate. Therefore, further research is essential in order to develop the SERS substrate with ultra-high sensitivity and selectivity by fabricating the appropriate substrate to achieve strong coupling between LSPs using defect engineered graphene.

In order to achieve strong EM enhancement, we have fabricated a reliable SERS- active substrate by decoration of defect-engineered CVD graphene with gold nanoparticles (Au NPs). It is well known that the local electric field enhancement depends on the particle size, shape and also the

gap between the particles in order to get the Raman signal enhancement in SERS [10]. To achieve the Raman signal enhancement and to control the distance between the Au NPs, we have used a plasma treatment strategy to create structural defects in graphene. Experimentally, it has been observed that Au NPs are stabilized at graphene defect sites and the defects can enhance the physical functionalization of metal NPs [25-27]. Here we focus on the EM enhancement by controlling the nanoparticle size and the gap between them on the defect engineered graphene substrate, where we believe the enhancement is mostly due to coupling of LSPs. In the light of the above, we have used the plasma treatment of monolayer graphene to create defects, such as carbon vacancies, on the graphene surface. The gas ($Ar/H_2$) flow rate, exposure time, and plasma power were adjusted to avoid the complete etching of the graphene. Au NPs were deposited on defect engineered graphene layers by electrodeposition. Quantitative analysis of the defect density, and the nature of the interaction of Au with graphene, was performed using Raman spectroscopy. In addition, the substrates thus prepared have been used to detect a dye molecule (Rhodamine B, RhB) and explore the Raman enhancement mechanisms.

## 2. Experimental Section

### 2.1. CVD growth of graphene and transfer process

Graphene films were grown on polycrystalline copper (Cu) foils (Sigma Aldrich, 25 μm thick, 99.98% pure) at 1000 $^oC$ in an electric tube furnace under high vacuum (~ $1\times10^{-4}$ mbar). Prior to the growth, Cu foils (3×3 $cm^2$) were cleaned with acetone, isopropyl alcohol (IPA) and deionized water (DI) to remove the organic and oxide impurities on the Cu foil. After cleaning with deionized water (DI), the Cu foils were dipped in diluted hydrofluoric acid (1% HF in DI) to remove the native oxide of copper. Finally, foils were dried under a $N_2$ flow and pressed between two clean glass slides to keep them as flat as possible. Then, the Cu foils were inserted into a quartz chamber and the chamber was purged with argon gas (100 SCCM) for 15 minutes. After filling the chamber with the argon, the argon gas was pumped out and the pressure was reduced to a high vacuum level (~ $1\times10^{-4}$ mbar). Later, the furnace temperature was raised to 1000 $^oC$ within 40 minutes and the temperature was kept constant for another 2 hours. A typical growth procedure is: (a) Cu foils were pre-annealed

in a $H_2$ environment (100 SCCM) for 1 hour in order to increase the grain size and avoid the oxidation of the copper; (b) initiation of the reaction by introducing $CH_4$ (25 SCCM) and $H_2$ (40 SCCM) at 1000 $^oC$, maintaining under reaction conditions for 1 hour; (c) cooling down the furnace to room temperature by purging with $H_2$ (40 SCCM) gas. As graphene was deposited on both sides of the copper foil, the graphene layer on the back of the foil was etched using oxygen plasma. The top layer was transferred to various substrates such as $SiO_2$/Si, quartz, and a Cu TEM grid by a wet transfer process. In this process, poly (methyl methacrylate) (PMMA)/anisole solution was spin coated on graphene/Cu foil (4500 rpm for 30 sec) and the copper was etched in aqueous 0.5 M ammonium persulfate solution. After complete etching of copper, the floating PMMA/graphene film was transferred to fresh ultra-pure water several times to rinse the etchant and copper residues. After rinsing, the PMMA/graphene was scooped and transferred on to the required substrates. After transferring the layer, the substrate was dried in the oven at 90 $^oC$, which also enables the flattening of the graphene film. Further, the PMMA was removed with hot acetone and isopropyl alcohol. Though wet transfer is a well-established process, it is known that significant PMMA and metal impurities remain on the graphene. In order to improve the quality of the graphene and to remove the residual impurities, substrates were annealed at 400 $^oC$ in the presence of $H_2$ gas for 2 hours.

### 2.2. Plasma treatment

The Ar/$H_2$ plasma treatment was carried out using an inductively-coupled RF plasma system. Before plasma treatment, the chamber was pumped down to $1\times10^{-7}$ mbar. The argon and hydrogen gas flux was controlled very precisely in the chamber using mass flow controllers. At first, the chamber was purged and pumped out with argon gas (99.999%) several times after loading the samples into the chamber and then the high vacuum ($1\times10^{-7}$ mbar) was created to avoid any cross contamination in the chamber. After plasma treatment we again used high purity argon gas (99.999%) to vent the chamber. A plasma power of 20 W was used, and the exposure time was varied from 2 sec to 15 sec. All the remaining plasma parameters, such as gas flux (Ar 90%, $H_2$ 10%), plasma power (20 W), and chamber pressure (10 mTorr), were kept constant throughout the experiment.

### 2.3. Electrodeposition of gold nanoparticles

Electrodeposition was used to deposit the Au NPs on graphene due to the advantage of greater control over the size of the NPs. Particle size can be controlled by tuning the charge passed and potential applied through the electrodes [28, 29]. The electrodeposition solution was prepared by dissolving 5 mM $HAuCl_4$, 6 M LiCl, 0.05M HCl in ultra-pure (Millipore Ultra) water. The optimized electrolyte concentrations and deposition conditions given in our recent report were employed [30]. Electrodeposition was carried out using a conventional three-electrode configuration with the CVD graphene as the working electrode, a length of platinum (Pt) wire (0.1 mm diameter, 99.99%, Advent) as a counter electrode, and polyester insulated Pt (0.125 mm diameter, 99.99%, Goodfellow; ca. 5 mm exposed Pt at the end) as a pseudo-reference electrode. Cyclic voltammetry (CV) was performed to find the optimum potential for the deposition (Figure (S1)). The CV was recorded from −1.0 V to 0.6 V vs. the Pt quasi-reference electrode at a 20 mV $s^{-1}$ scan rate. The CV shows two anodic peaks (labelled as A1 & A2) and two cathodic peaks (labelled as C1 & C2). The C1 and A1 peaks are comparatively sharp, whereas the C2 and A2 peaks are broad. The C1 occurs at −0.27 V and the C2 reduction peak occurs at −0.96 V on graphene. It is clear that the current on the reverse scan is greater than that for the forward scan. The observed large current in the reverse scan is due to the continuous growth of NPs. From CV we have chosen the optimum reduction potential of −0.96 V and deposited the Au NPs using chrono-amperometry. Au NPs were deposited in a controlled way for 3 sec. The spontaneous formation of gold on graphene should be avoided in order to control the particle size and morphology. The required reduction potential (−0.96 V vs. Pt) was applied to the cell before introduction of the electrolyte to avoid the spontaneous Au deposition.

### 2.4. Characterization

Electrodeposition experiments were carried out using a potentiostat/galvanostat (Autolab, Metrohm Instruments, model 302N) at room temperature employing the conventional three-electrode cell configuration. Raman measurements were done on a high resolution Renishaw inVia™ confocal Raman system in backscattering geometry using the 532 nm and 633 nm (He–Ne laser) excitation wavelengths. Raman mapping measurements were carried out in the 10 μm × 10 μm frame size on the samples at 532 nm laser excitation. The optical properties of the samples were measured by a

Lambda950-Perkin Elmer UV-visible absorption spectroscopy system. The contact angle measurements were recorded using 1 μL droplets of water in air. The images were recorded and analysed by Theta Optical Tensiometer (Biolin Scientific, Sweden) running OneAttension software (version 2.3) based on the Young-Laplace equation. Scanning electron microscopy (SEM) was performed using a FEI Quanta 650 FEG environmental scanning electron microscope (operating voltage 0.5–30 kV). X-ray photoelectron spectroscopy (XPS) was performed with a KratosS5 Axis Ultra DLD spectrometer using the Al $K_\alpha$ X-ray source (1486.6 eV). The XPS measurements were performed at zero take-off angles from the CVD grown graphene transferred onto $Si/SiO_2$ substrates. High resolution and survey spectra were recorded with pass energies of 20 eV and 80 eV, respectively. The crystallinity and structural defects of graphene layers were identified using bright field scanning transmission electron microscopy (STEM) mode using an aberration-corrected STEM (JEM 2100F, 200 kV).

## 3. Results and Discussion

The density of defects (particularly carbon vacancies) and the degree of disorder in single layer graphene (SLG), with and without plasma treatment, were estimated using Raman spectroscopy. This technique is very sensitive to the in-plane defects and is able to probe the nature of defects in SLG based on the line shapes and integrated intensity ratios of Raman finger prints, such as D, G and 2D Raman bands. The forbidden D and D' Raman bands appear in the spectrum in order to conserve the momentum when the defects (carbon vacancies) are present in the sample. The small shoulder observed at the higher frequency side of the G band (1620 $cm^{-1}$) is called the D' band, and mainly originates from edges or the structural disorders in graphene [31, 32]. Figure (1) shows the comparison of the Raman spectra of pristine and plasma treated graphene films before and after Au electro-deposition. The D peak is not visible in the pristine graphene (GR), which indicates that the quality of the graphene is high (Figure (1a)). The two sharp peaks at 1580, 2685 $cm^{-1}$ (G and 2D, respectively) observed and the line shape evolution (lower FWHM ~26.3 $cm^{-1}$) of the 2D band indicates that a graphene sheet consists of a single layer [31, 32]. Figure (S2) shows the characteristic Raman modes of SLG after $Ar/H_2$ plasma treatment as a function of plasma exposure time. It is observed that the D

peak intensity increases with the plasma exposure time, which indicates a gradual increase in the number of defects introduced to the graphene lattice. For example, the $I_D/I_G$ ratio in the case of 15-sec exposure sample (GR15) is 2.31, indicating that the plasma exposure process has altered the structure of SLG with more structural defects, particularly carbon atom vacancies within the graphene layer. The relative integrated intensity ratio of $I_D/I_G$ bands is remarkable even for the shorter exposure time (Figure S2). On the other hand, the intensity of the D' band also increases with plasma exposure time. To understand this behaviour, some consideration is required of the mechanism of disorder production during plasma treatment. The D and D' peaks appear for two reasons: (1) the order of pristine C atoms in graphene is interrupted by the plasma and some of the C atoms may be sputtered out, which is named the ion bombardment effect [33]. The sputtered C atoms create vacancies in the lattice and these vacancies increases with the exposure time and finally create edge sites in the graphene, (2) formation of a covalent bond with the graphene lattice during plasma treatment, leading to functionalization or surface modifications [34, 35]. Both these processes contribute to the defect peak in the graphene. In our case, the bombardment effect might be the reason for observing these two peaks, rather than functionalization. In order to calculate the inter-defect density ($n_D$) and areal defect density ($L_D$) from the $I_D/I_G$ ratio, we have used the empirical relations proposed by Cançado *et al* [36].

$$L_D^2(nm^2) = (1.8 \pm 0.5) \times 10^{-9}(\lambda_L^4)\left(\frac{I_D}{I_G}\right)^{-1}$$

$$n_D(\mu m^{-2}) = \frac{(1.8 \pm 0.5)}{\lambda_L^4} \times 10^{14}\left(\frac{I_D}{I_G}\right)$$

Where $\lambda_L$ is the excitation wavelength in nm. The sharp G and 2D bands (intensity ratio $I_{2D}/I_G$ = 2) and the absence of the D band in graphene are significant for perfect $sp^2$ crystallinity with monolayer coverage of graphene. The $n_D$ and $L_D$ values were deduced using the above equations for all the plasma treated samples, and the results are summarized in Table (S1).

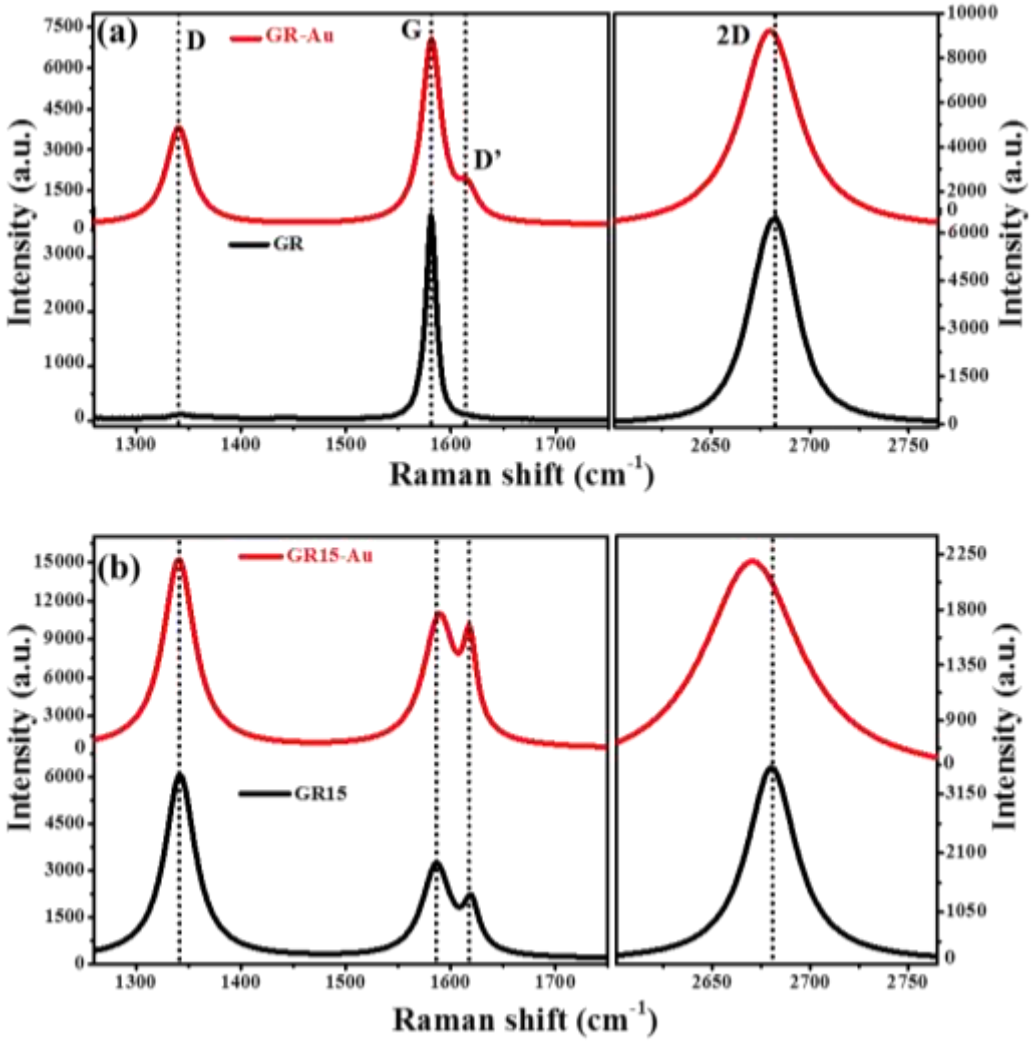


**Fig. 1** Comparison of the Raman spectra of (a) pristine and (b) plasma treated graphene films before and after Au electrodeposition.

After Au deposition (GR15-Au), it is observed that there is a shift in G and 2D peak positions which indicates the functionalization of graphene with Au NPs (Figure (1b)) [37]. Moreover, there is no substantial change in D and D' bands FWHM and peak positions after Au deposition but it is clear that there is a huge enhancement in both D and D' peak intensities after Au deposition. The observed 2D peak FWHM (~70 $cm^{-1}$) of Au deposited GR is similar to that of pristine bilayer graphene (BLG) [31]. This means that the Au deposited SLG behaves like a pristine BLG. It is observed that the FWHM of GR-Au 2D peak increases because the Au atoms diffuse into the graphene layer due to the presence of structural defects.

Raman mapping was performed for the defective graphene samples before and after Au deposition. The well-known D, G, and 2D bands were mapped to assess the surface coverage, uniformity of the graphene layer and also the interaction of Au with the graphene. Figure (2) illustrates the areal integrated intensity maps of various Raman modes of graphene before and after Au electrodeposition in the scanning area of 10×10 $\mu m^2$. Figure (2a-2c) shows the Raman mapping images of D, G, and 2D bands before Au deposition on GR15 sample. The relative areal intensity maps of D, G bands (intensity ratio of $I_D/I_G$ is 1.57 (Table S1)), which clearly indicates the presence of structural defects such as point, edge, and multi vacancies in graphene after plasma treatment (also confirmed from the STEM imaging, *vide infra*). Figure (2d-2f) shows the Raman mapping images of D, G, and 2D bands after Au deposition on GR15 sample (GR15-Au). After Au deposition, the $I_D/I_G$ ratio increased from 1.57 to 2.60, which clearly reveals the interaction of graphene with Au. Moreover, it also reveals the role of graphene structural defects for the formation and stabilization of Au NPs. The higher intensity of the D band compared to the 2D band indicates that the Au NPs are attached at graphene defect sites [26]. Figure (S3) shows the relative areal intensity maps of the G and 2D bands of pristine graphene before and after Au electrodeposition. The higher intensities and uniform intensity distribution of G and 2D bands confirms the large area coverage of single-layer graphene (SLG).

The observed enhancement in Raman signals might be due to two major contributions. One is the SPR effect of Au NPs in the locality of defects in graphene and the other reason is the enhanced defect density in plasma treated GR when compared to pristine GR. The Au induced enhancement is very strong in the D and D' bands, which suggests that the Au NPs preferentially grows at the graphene defect sites. The observed 2D peak intensity quenching in GR after Au deposition is due to the hybridization of Au *d* orbitals with the *2p* orbitals of graphene [37]. The hybridization of graphene with Au is further confirmed by XPS measurements.

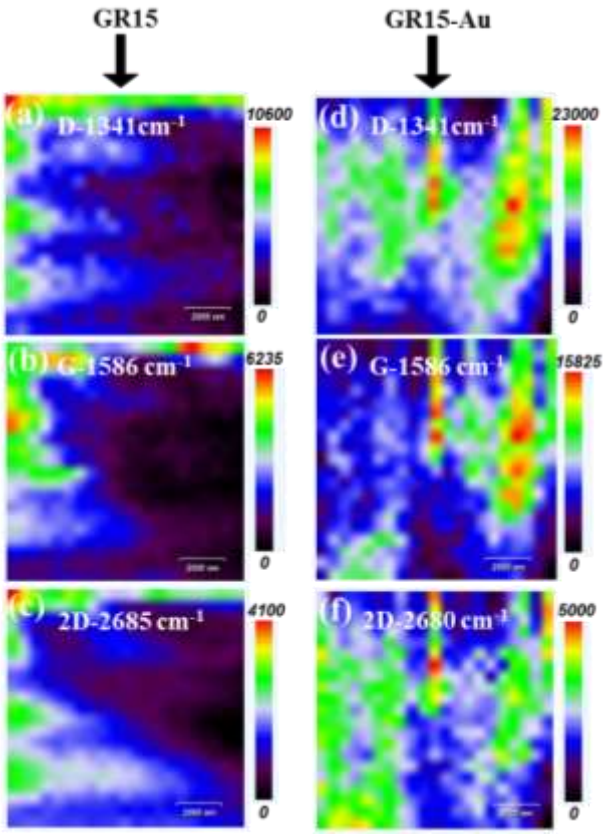


**Fig. 2** Raman mapping images for D, G, and 2D bands of GR15 films before and after Au deposition: (a-c) before gold deposition, (d-f) after gold deposition.

In order to understand the SPR effect on Raman enhancement of defective graphene, we have performed the optical absorption measurements of graphene on quartz substrates. Optical absorption measurements were carried out on GR15, GR15-Au, and GR15-Au-RhB on quartz substrates to understand the effect of Au functionalization on plasma treated graphene samples. Figure (S4a) shows the optical absorption spectra for plasma treated graphene samples. The absorption spectra for all the samples look identical and quite flat over the entire range of UV-Vis-NIR, though there are structural defects present on the graphene plane. Figure (3a) presents the comparison of the absorption spectra of the GR15 sample before and after Au electro-deposition. The GR15-Au absorption spectra show a strong absorption broadband, from the visible to near IR regions of the spectra, which is due to the surface plasmon resonance (SPR) effect from the Au NPs. The SPR band position is centred at 631 nm. It is observed that there is a stronger SPR absorption in plasma treated graphene sample compared to GR-Au. The observed strong enhancement in the SPR absorption might be due to the

strong plasmonic coupling between the Au and defective graphene. There is an upshift and broadening observed in the SPR absorption band in plasma treated samples (Figure S4b). The redshift is due to change in the refractive index of the surrounding dielectric medium of Au NPs on graphene [38]. The peak broadening in our case might be due to the formation of longer Au-C bonds: diffusion of the Au atoms in graphene results in the formation of longer Au-C bonds [39]. The effect of RhB dye on the GR-Au substrate has been evaluated (Figure (3a)). It is clear that the RhB dye ($10^{-2}$ M aqueous RhB solution drop cast on to Au-Graphene/Quartz substrate for the absorbance measurement) shows an absorption peak at 560 nm along with the Au SPR band. The higher optical absorption is observed for the GR15-Au treated sample. The observed higher optical absorption might be due to the well-controlled inter-defect distance which will help to couple the LSPs. The strong coupling of LSP might be the reason for the strong SERS enhancement in defective Gr-Au samples.

Surface properties of the graphene have been studied using water in air contact angle measurements in order to understand the effect of plasma treatment. Figure (3b) shows the variation of water contact angle on graphene/$SiO_2$ (300 nm)/Si with plasma exposure time. The contact angle was drastically changed from 91° to 52°. Figure (3b) also shows that the contact angle decrease correlates with the increase in the $I_D/I_G$ ratio. The decrease in the contact angle and increase in the $I_D/I_G$ ratio indicates that the defects, which might be vacancies or surface corrugation, have increased the polarity of the graphene surface. To further understand and correlate the contact angle data, XPS measurements were performed. XPS data (Figure 4) shows that the intensity of the C-C, C-O features increasing with the plasma exposure time (*vide infra*). These results indicate that the observed hydrophilicity after the plasma treatment is due to the formation of C-C and C–O bonds.

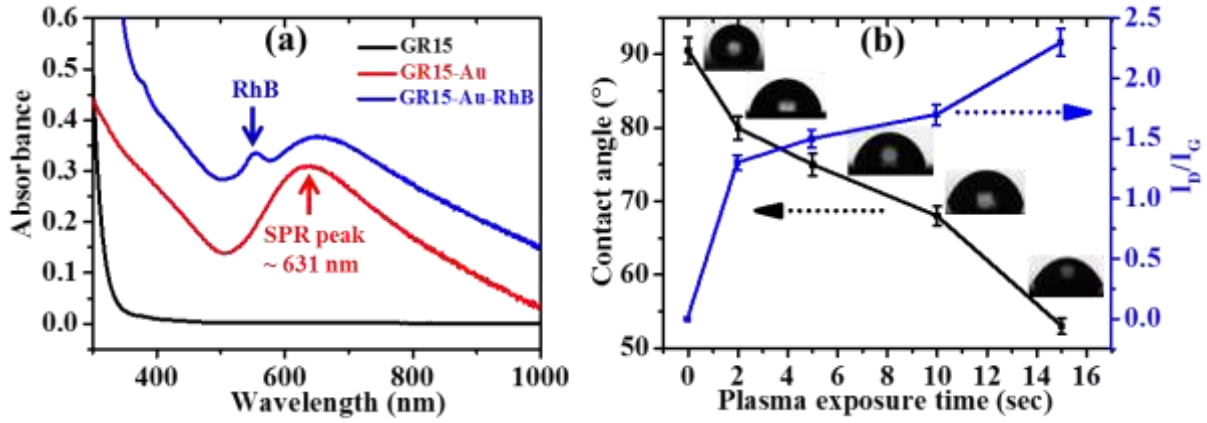


**Fig. 3** (a) Comparison of the optical absorption spectra of GR15, GR15-Au, and GR15-Au-RhB films measured on quartz substrate. A strong surface plasmon resonance absorption peak is observed in GR15-Au. (b) Variation of graphene water contact angle and $I_D/I_G$ ratios with different plasma treatment times. The insets show the corresponding contact angle photographs.

SEM surface morphology was carried out to check the distribution of the Au NPs at defect sites on the graphene surface (Figure (4)). Figure (4a) shows the wrinkles in the pristine GR. Figure (4b) shows the distribution of NPs at the edges and in the basal plane of graphene. Figure (4c) shows the Au NPs distribution on the plasma treated GR15-Au sample. It is clear that the coverage of the Au NPs is higher in defective samples (GR15-Au) as compared to pristine GR. This indicates that the Au NPs are preferentially attached to the defect sites and the higher coverage can be attributed to the relative ease of nucleation on defect sites. Further, XPS measurements were carried out to confirm the Au functionalization on graphene. Figure (4d-4f) shows the high-resolution core level C-1s spectra of graphene before and after Au electrodeposition. In pristine GR (Figure (S5)), the C-1s peak is deconvoluted into two peaks. The most dominant component, located at ~284.37 eV corresponding to the C=C ($sp^2$) bond, arises from the carbon atoms in the honeycomb lattice [40-42]. The small shoulder peak fitted at 290.7 eV corresponds to the π-π* interaction of aromatic C=C bonds [40-42]. The high-intensity sharp peak with a much smaller FWHM (0.5 eV), and the absence of any C-C ($sp^3$) peak, confirms the high quality of graphene (Table S2) [40-42]. Figure (4d) represents the core level C-1s spectra of the GR15 sample. The spectrum is deconvoluted into four peaks. The four peaks located at binding energies of 284.4, 285.1, 286.3, and 288.7 eV can be assigned to C=C ($sp^2$), C-C ($sp^3$), C-O,

and C=O, respectively (Table (1)) [40-42]. After plasma treatment, the C-C ($sp^3$) peak is prominent, due to the formation of structural defects such as point, edge, and multi-carbon vacancies in the graphene. This observation is also consistent with the Raman and STEM measurements. Moreover, the presence of the low-intensity shake-up peak at 292.8 eV is ascribed to the π-π* interaction of $sp^2$ hybridized carbon atoms. The presence of oxygen functional groups and their linewidths indicates that the native oxygen is attached to the $sp^3$ sites of graphene which might be due to room temperature storage of samples. Figure (4e) represents the core level C-1s spectra of the GR15-Au. As shown in Figure (4d, 4e), the C-1s spectra of GR15 and GR15-Au show a similar shape, also indicating the main C-C ($sp^2$) component and low concentration of other carbonaceous species. After Au deposition, the C-1s spectra show a broadening of both the $sp^2$ and $sp^3$ bands. The changes in the peak parameters attained from the peak fitting are summarized in Table 1. The observed changes in the C-1s core level spectrum (intensities and FWHM changes) before and after Au deposition also suggest a significant character of the charge-transfer (CT) between graphene and Au [37]. Moreover, it clearly demonstrates the dominance of $sp^3$ hybridization in Au-decorated GR. Figure (4f) shows the Au4f spectra after functionalizing the plasma treated graphene sample with gold. The spectrum shows two doublets at 83.08 eV and 86.78 eV corresponding to $4f_{7/2}$ and $4f_{5/2}$ states, respectively. The peak separation of 3.7 eV and the $4f_{7/2}$ peak position at 83.08 eV confirms the presence of Au (0) [43]. XPS survey scan measurements were carried out in order to calculate the O/C ratios in graphene (on the $SiO_2$/Si substrate) before and after plasma treatment, as shown in Figure S6. The Si and O peaks in Figure S6 arises from the $SiO_2$/Si substrate, while the C-1s peak is due to the presence of graphene. It is observed that the O/C ratio is increased with the plasma exposure time from 0.47% to 1.0%. This increment is due to the adsorption of oxygen at the $sp^3$ defect sites of graphene after plasma treatment. However, the O/C ratio was decreased after gold electrodeposition. These XPS results clearly indicate the functionalization of graphene with Au due to the presence of structural defects and are in agreement with the Raman measurements.

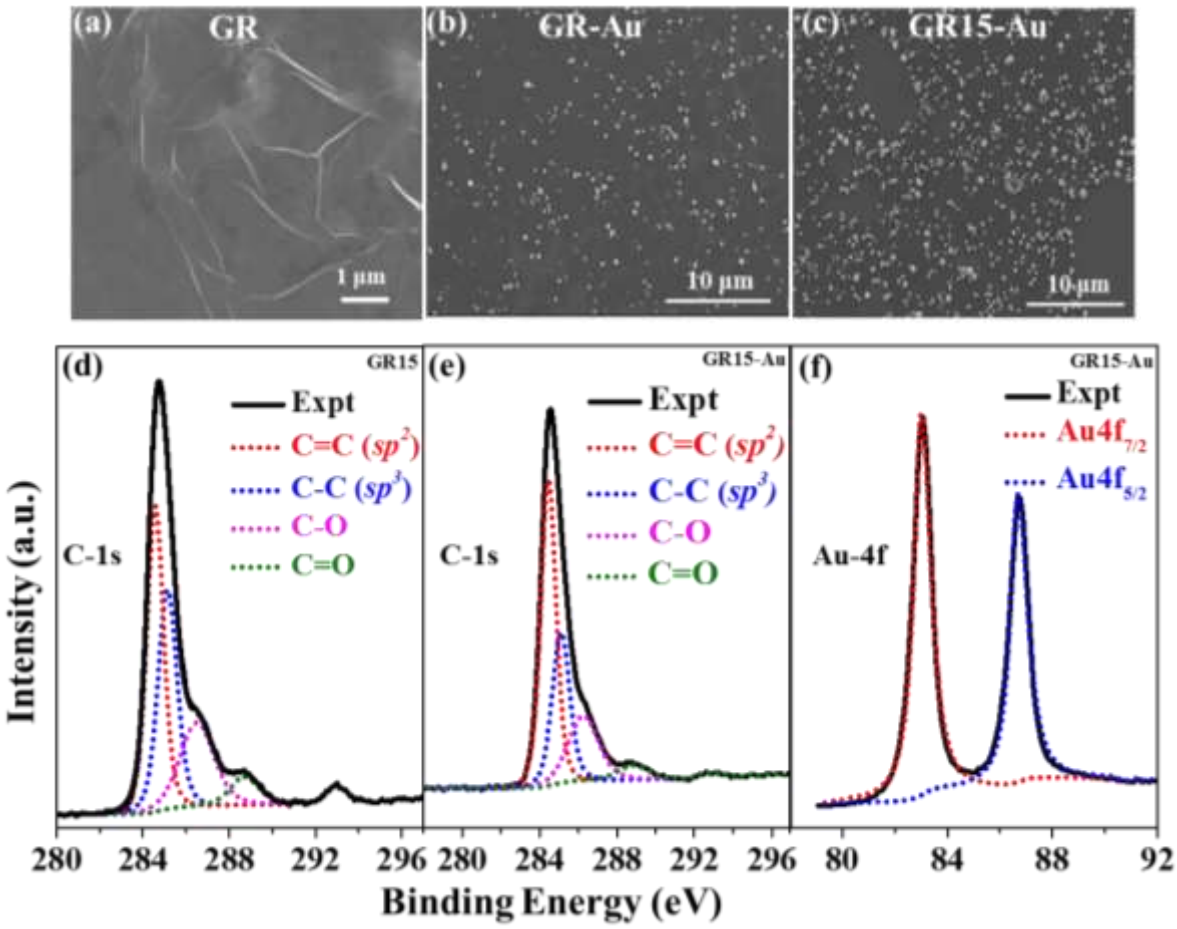


**Fig. 4** SEM surface morphology images of (a) GR, (b) GR-Au, and (c) GR15-Au samples. XPS spectra of (d) GR15 C-1s, (e) GR15-Au C-1s, and (f) GR15-Au Au-4f.

**Table 1.** Fitting parameters of the C-1s core level XPS spectra of GR15 and GR15-Au samples.

| | GR15 | | | GR15-Au | | |
|---|---|---|---|---|---|---|
| Band | Peak | FWHM | Intensity | Peak | FWHM | Intensity |
| C=C $sp^2$ | 284.46 | 0.91 | 5540 | 284.56 | 1.24 | 7935 |
| C-C $sp^3$ | 285.11 | 1.04 | 4247 | 285.14 | 2.86 | 4050 |
| C-O | 286.30 | 1.80 | 2218 | 286.50 | 0.65 | 2180 |
| C=O | 288.71 | 1.58 | 1382 | 288.84 | 1.39 | 1070 |
| π-π* | 292.80 | 1.03 | 1288 | 292.90 | 1.14 | 928 |

To investigate the morphological features and directly visualize plasma-induced defects of plasma treated GR samples, we used the STEM imaging technique. Moreover, this technique is also

useful to assess the homogeneity and number of layers in graphene. Figure (5a) shows the STEM bright field (BF) image of graphene (GR) on a copper grid. Figure (5b) shows BF STEM images of graphene after 15-sec plasma treatment (GR15). In Figure (5a, 5b) one can see that with the increase of plasma exposure time, the number and type of defects increased. The arrows indicate the various kind of structural defects present on a graphene layer such as single point defects (vacancies of C atoms, white arrows) and multi vacancies (yellow arrows). Figure (5c, 5d) show the BF STEM images of Gr with Au modified substrates.

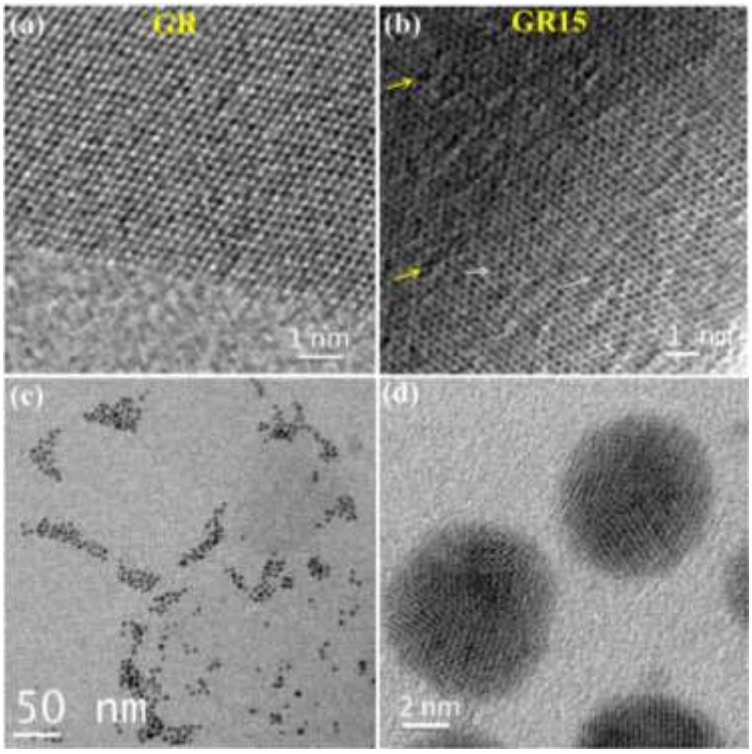


**Fig. 5** Bright field STEM images of (a) GR and (b) GR15 sample. White arrows indicate single point defects (vacancies of C atoms) and yellow arrows multi vacancies on graphene. (c) Bright field STEM image of Au NPs on GR15 sample and (d) corresponding high resolution image of Au NPs on GR15.

The SERS characteristics of the Gr-Au modified substrates were investigated by using RhB as a Raman-active probe molecule. In a representative experiment, 10 μL of an aqueous analyte solution was drop cast on the substrates. Note that the intensity of the incident laser power, acquisition time, and number of accumulations were carefully adjusted by trial and error in order not to damage the samples during exposure, since beam damage is one of the common problems in graphene SERS. However, we observed that the Raman spectra were quite stable up to 2.0 mW laser power for several

times of exposure. We conducted SERS measurements using optimized parameters at which we noticed no beam damage of the samples (power 0.3 mW, exposure time: 1 sec, grating: 600 lines/millimetre, objective: 50×). No obvious damage to the probe molecule was noticed, the only issue that was observed at higher power (>2.0 mW) and longer exposure time (>2 sec) was the saturation of the Raman signal. Figure (6) shows the Raman spectra of RhB, obtained on Gr-Au and GR15-Au substrates at an excitation wavelength of 633 nm. Whereas no Raman signals were detected when $10^{-3}$ M analyte solution was deposited on bare Si (001) substrate (Figure S8a). Figure (6a) shows the Raman spectra of the RhB molecules deposited on the pristine GR-Au substrate without plasma treatment at concentrations in the range from $10^{-6}$ to $10^{-16}$ M. The pristine GR-Au substrate can detect the RhB Raman signals over a concentration range spanning $10^{-6}$ to $10^{-12}$ M, but below $10^{-12}$ M the peaks were absent. From Figure (6), it can be observed that there is a quenching in the fluorescence background of the RhB and shows its Raman signature peaks along with graphene peaks. The major characteristic Raman peak at 1,651 $cm^{-1}$ was selected to calculate the enhancement factor (EF) of the plasma modified graphene-gold substrate. Further, the SERS enhancement was investigated on various plasma treated graphene gold substrates for various analyte concentrations (all spectra measured with a 633 nm laser and the laser power is 0.3 mW). Significant Raman signals were detected for the same solution and, on progressive dilution, even for $10^{-16}$ M concentrations of RhB when deposited on Gr15-Au substrate, with a good signal-to-noise ratio and peak positions consistent with earlier reports. Among all the samples, the GR15-Au substrate shows the highest SERS enhancement with high signal reproducibility over a large area even for laser power of 0.3 mW (Figure (6b)). From figure (6) it is clear that the Raman signals of RhB molecules on all the plasma treated samples are enhanced, apparently with the further suppression of fluorescence background of RhB compared to that of RhB on a pristine GR-Au substrate. Table 2 compares the performance of graphene-metal based SERS substrates reported in literature with our results. Most of the studies on graphene-metal based substrates reported detection limits were in the range of $10^{-6}$ M to $10^{-10}$ M [44-54]. But the substrates presented in this work can able to detect ultra-low concentrations ranging from $10^{-6}$ to $10^{-16}$ M with reliable and a good signal-to-noise ratio. The value of the SERS enhancement factor (EF) is $6.93\times10^{8}$ (the details of the EF calculations are provided in the SI) for the GR15-Au

sample. There are two different factors contributing to this enhanced Raman signals on GR15-Au substrates. As per the previous reports, the structural disorder can generally introduce local dipoles leading to the improved SERS effect [55, 56]. As graphene monolayer thickness is in the sub-nanometer scale and its structure can be easily modified with the plasma treatment, hence the generated structural disorder induced dipole and the strong resonance energy transfer between Au NPs and graphene might be the driving force for the SERS enhancement. In our samples, the SPR coupling might be strong as the distance between the Au NPs were controlled by controlling the defects in graphene. Moreover, we showed above that the inter-defect distance and density of defects are increasing with plasma exposure time. As related to the Au induced enhancement in G and 2D bands, stronger enhancement in D and D′ bands is suggestive of preferential deposition of Au NPs at the defect sites and an SPR enhancement effect in the Raman spectra.

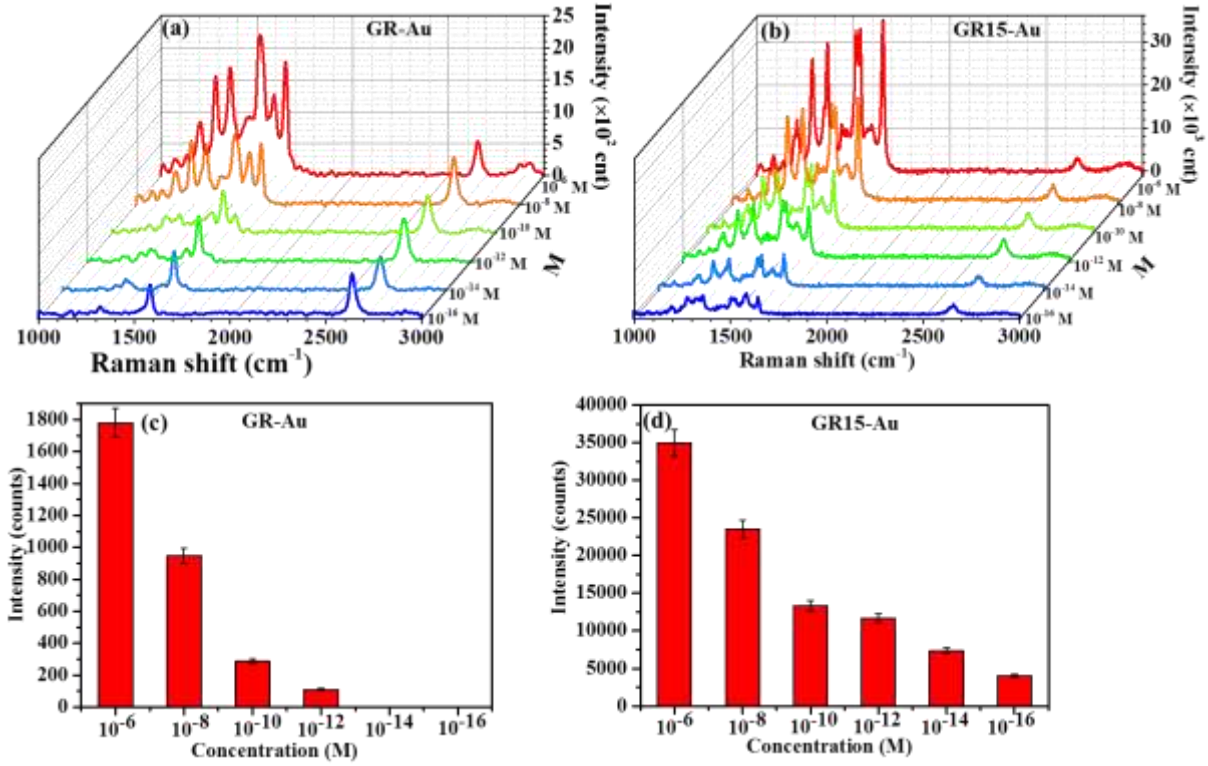


**Fig. 6** SERS response and molecular detection of graphene-gold modified substrates: (a) SERS spectra of RhB on GR-Au films from a $10^{-6}$ – $10^{-16}$ M concentration range, (b) SERS spectra of RhB on GR15-Au substrate. SERS intensities at 1,651 $cm^{-1}$ for RhB concentration ranging from $10^{-6}$ to $10^{-16}$ M for (c) GR-Au and (d) GR15-Au substrates. The error bars indicate standard deviations from

at least eight spectra for the RhB concentrations of $10^{-6}$–$10^{-10}$ M and five spectra for the RhB concentrations of $10^{-12}$–$10^{-16}$ M.

**Table 2.** Comparison of our current results on SERS response with previous reports on graphene-metal based SERS substrates.

| **SERS substrate** | **Graphene preparation** | **Detection limit** | **EF (analyte)** | **Reference** |
|---|---|---|---|---|
| Au NPs/Gr/$SiO_2$/Si | CVD | $10^{-16}$ M | $6.93\times10^{8}$ (RhB) | This work |
| Au or Ag metal nano-islands/Gr/$SiO_2$/Si | CVD | $10^{-5}$ M | -- (CuPc & R6G) | 44 |
| 3D crumpled Gr−Au NPs | CVD | $10^{-10}$ M | -- (4mercaptophenol) | 45 |
| Si/Gr/Au NP substrate | CVD | $8\times10^{-7}$ M | -- (R6G) | 46 |
| Gr-wrapped Cu NPs | CVD | $5\times10^{-9}$ M | -- (Adenosine) | 47 |
| Cu/Gr/Cu NPs | CVD | $0.5\times10^{-9}$ M | $1.89\times10^{7}$ (CuPc) | 48 |
| Gr-encapsulated Cu NPs | CVD | $10^{-10}$ M | -- (R6G) | 49 |
| Cu/Gr/Gr@Cu NPs | CVD | $10^{-9}$ M | -- (R6G) | 50 |
| Cu/Gr double-nanocaps | CVD | $10^{-10}$ M | -- (R6G) | 51 |
| Gr–AuNP hybrid film | CVD | $1.0\times10^{-8}$ M | $10^{7}$ (R6G) | 52 |
| Gr-encapsulated Au NPs | CVD | $10^{-6}$ M | $6.87\times10^{5}$ (MB) | 53 |
| Au/Gr/Cu hybrid | CVD | $0.1\times10^{-9}$ M | $10^{6}$ (RhB and R6G) | 54 |

## 4. Conclusions

Plasma modification is described as a strategy to prepare gold-functionalised graphene for surface-enhanced Raman scattering, using the RhB molecule as a “model” analyte. We have demonstrated that it is possible to tune the EM and CM enhancements via the plasma modification strategy. The structural induced defects in graphene by plasma treatment along with Au NPs functionalization resulted in high SERS enhancement. Based on the SERS measurements, plasma modified GR15-Au substrate showed very low detection limits ($10^{-16}$ M) and high Raman signal enhancements (EF~ $6.93\times10^{8}$) compared to pristine GR-Au. The observed enhancement in the SERS

might be due to the structural disorder induced generation of local dipoles and the strong resonance energy transfer between Au NPs and graphene. Moreover, we also observed the strong quench in the background fluorescence signal from the Au and probe molecules due to the graphene. Hence, the defect-mediated efficient gold functionalization and easy charge transfer at the graphene/Au interface is expected to be suitable for biosensing and Raman imaging applications. These results should open pathways for the development of next-generation SERS based biosensors and bio-imaging applications using graphene and other 2D nanomaterials through functionalization with noble metal NPs.

**Acknowledgements**

B.A would like to thank National Graphene Institute (NGI) for providing access to facilities. R.A.W.D acknowledges funding from the EPSRC "2D health" project; grant reference EP/P00119X/1. W.T and R.K.B acknowledge the Marie-Sklodowska-Curie individual fellowship under EU H2020 Programme (H2020-MSCA-IF-2017; Grant No: 750929).

**References**

(1) S.D. Hudson, G. Chumanov, *Anal. Bioanal. Chem*. **2009**, *394*, 679.

(2) W.F. Pearman, A.W. Fountain, *Appl. Spectrosc*. **2006**, *60*, 356.

(3) R.A. Halvorson, P.J. Vikesland, *Environ. Sci. Technol*. **2010**, *44*, 7749.

(4) M. Yilmaz, E. Babur, M. Ozdemir, Rebecca L. Gieseking, Y. Dede, U. Tamer, G. C. Schatz, A. Facchetti, H. Usta, G. Demirel, *Nat. Mater*. **2017**, *16*, 918.

(5) S. Schlücker, Angew, *Chem. Int. Ed.* **2014**, *53*, 4756.

(6) J.R. Lombardi, R.L. Birke, *Acc. Chem. Res*. **2009**, *42*, 734.

(7) X.M. Qian, S.M. Nie, *Chem. Soc. Rev*. **2008**, *37*, 912.

(8) J.R. Lombardi, R.L. Birke, *J. Phys. Chem. C.* **2008**, *112*, 5605.

(9) J. Liao, J. Li, J. Zhang, N. Gao, P. Li.1, K. Huang , E. T. Yu, J. Kang, *Nanoscale Res Lett*. **2018**, *13*,280.

(10) E.C. Le Ru, P.G. Etchegoin, Principles of Surface-Enhanced Raman Spectroscopy, 1st Edition, *Elsevier*. **2009**, Amsterdam.

(11) F. Schedin, E. Lidorikis, A. Lombardo, V. G. Kravets, A. K. Geim, A. N. Grigorenko, K. S. Novoselov, A. C. Ferrari, *ACS Nano.* **2010**, *4*, 5617.

(12) Y. Wu, J. Niu, M. Danesh, J. Liu, Y. Chen, Lin Ke, C. Qiu, and H. Yang, *Appl. Phys. Lett.* **2016**, *109*, 041106.

(13) B. Vasic, Goran Isic, Ra. Gajic, *J. Appl. Phys.* **2013**, *113*, 013110.

(14) X. Ling, L. Xie, Y. Fang, H. Xu, H. Zhang, J. Kong, M.S. Dresselhaus, J. Zhang, Z. Liu, *Nano Lett*. **2010**, *10*, 553.

(15) X. Ling, L.G. Moura, M.A. Pimenta, J. Zhang, *J. Phys. Chem. C*. **2012**, *116*, 25112.

(16) S. Huang, X. Ling, L. Liang, Y. Song, W. Fang, J. Zhang, J. Kong, V. Meunier, M. S. Dresselhaus, *Nano Lett.* **2015**, *15*, 2892.

(17) V. Giannini, A. Berrier, S. A. Maier, J. A. Sánchez-Gil, J. G. Rivas, *Opt. Express.* **2010**, *18* 2797.

(18) Z. Fei, G. O. Andreev, W. Bao, L. M. Zhang, A. S. McLeod, C. Wang, M. K. Stewart, Z. Zhao, G. Dominguez, M. Thiemens, M. M. Fogler, M. J. Tauber, A. H. Castro-Neto, C. N. Lau, F. Keilmann, and D. N. Basov, *Nano Lett*. **2011**, *11*, 4701.

(19) L. Ju, B. Geng, J. Horng, C. Girit, M. Martin, Z. Hao, H. A. Bechtel, X. Liang, A. Zettl, Y. R. Shen, and F. Wang, *Nat. Nanotechnol*. **2011**, *6*, 630.

(20) J. Chen, M. Badioli, P. Alonso-Gonza´lez, S. Thongrattanasiri, F. Huth, J. Osmond, M. Spasenovic, A. Centeno, A. Pesquera , P. Godignon , A. Z. Elorza, N. Camara, F. Javier Garcı´a de Abajo , R. Hillenbrand, F. H. L. Koppens, *Nature***. 2012**, *487*, 77.

(21) H.G. Lai, F. Xu, Y. Zhang , L. Wang, *J. Mater. Chem. B*. **2018**, *6*, 4008.

(22) M. C. Dalfovo, G. I. Lacconi, M. Moreno, M. C. Yappert, G. U. Sumanasekera, R. C. Salvarezza and F. J. Ibañez, *ACS Appl. Mater. Interfaces*. **2014**, *6*, 6384.

(23) S. Feng, M. C. dos Santos, B. R. Carvalho, R. Lv, Q. Li, K. Fujisawa, A. Laura Elías,Y. Lei, N. Perea-López, M. Endo, M. Pan, M. A. Pimenta, M. Terrones, *Sci. Adv*. **2016**, *2*, 1600322.

(24) S. Huh, J. Park, Y. Soo Kim, K. S. Kim, B. H. Hong, Jwa-Min Nam, *ACS Nano*. **2011**, *5*, 9799.

(25) Q. Chen, K. He, A. W. Robertson, A. I. Kirkland, J. H. Warner, *ACS Nano*. **2016**, *10*, 10418.

(26) R. K. Biroju, P. K. Gi, *J. Phys. Chem. C*. **2014**, *118*,13833.

(27) R. K. Biroju, B. Choudhury, P. K. Giri, *Catal. Sci. Technol.* **2016**, *6*, 7101.

(28) E.C. Walter, B.J. Murray, F. Favier, G. Kaltenpoth, M. Grunze, R.M. Penner, *J. Phys.Chem. B.* **2002**, *106*, 11407.

(29) R.M. Penner, *J. Phys.Chem. B.* **2002**, *106*, 3339.

(30) D. J. Lomax, R. A.W. Dryfe, *J. Electroanal. Chem.* **2018**, *819*, 374.

(31) Y. Hao, Yi. Wang, L. Wang, Z. Ni, Z. Wang, R. Wang, C. Keong Koo, Z. Shen, John T. L. Thong, *Small*. **2010**, *6*, 195.

(32) L.M. Malard, M.A. Pimenta, G. Dresselhaus. M.S. Dresselhaus, *Physics Reports*. **2009**, *473*, 51.

(33) M.M. Lucchese, F. Stavale, E.H. Martins-Ferreira, C. Vilani, M. V. O. Moutinho, R.B. Capaz, C.A. Achete, A. Jorio, *Carbon.* **2010**, *48*, 1592.

(34) M. Ding, Y. Tang, A. Star, *J. Phys. Chem. Lett*. **2012**, *4*, 147.

(35) K. S . Subrahmanyam, A.K. Manna, S.K. Pati, C.N.R. Rao, *Chem. Phys. Lett.* **2010**, *497*, 70.

(36) Cancado, L. G, Jorio, A, Ferreira, E. H. Martins, Stavale, F, Achete, C. A, Capaz, R. B, Moutinho, M. V. O, Lombardo, A, Kulmala, T. S, Ferrari, A. C. *Nano Letters*. **2011**, *11*, 3190.

(37) P. R. Tulika, R. Laha, J. Balakrishnan, *J. Raman Spectrosc.* **2017**, *48*, 586.

(38) A. Sánchez-Iglesias, E. Carbó-Argibay, A. Glaria, B. Rodríguez-González, J. Pérez-Juste, I. Pastoriza-Santos and L. M. Liz-Marzán, *Chem. – Eur. J.* **2010**, *16*, 5558.

(39) H. Wang, Q. Wang, Y. Cheng, K. Li, Y. Yao, Q. Zhang, C. Dong, P. Wang, U. Schwingenschlögl, W. Yang and X. X. Zhang, *Nano Lett*. **2011**, *12*, 141.

(40) H. J. Shin, K. K. Kim, A. Benayad, S. M. Yoon, H. K. Park, I. S. Jung, M. H. Jin, H. K. Jeong, J. M. Kim, J. Y. Choi and Y. H. Lee, *Adv Funct Mater*. **2009**, *19*, 1987.

(41) N. J. Yang, C. G. Zoski, *Langmuir*. **2006**, *22*, 10338.

(42) C. Mattevi, G. Eda, S. Agnoli, S. Miller, K. A. Mkhoyan, O. Celik, D. Mostrogiovanni, G. Granozzi, E. Garfunkel and M. Chhowalla, *Adv Funct Mater.* **2009**, *19*, 2577.

(43) M.P. Casaletto, A. Longo, A. Martenara, A. Prestianni, A.M. Venezia, *Surf. Interface Anal*. **2006**, *38*, 215.

(44) W. Xu, X. Ling, J. Xiao, M. S. Dresselhaus, J. Kong, H. Xu, Z. Liu, J. Zhang, *Proc Natl Acad Sci*. **2012**, *109*, 9281.

(45) J. Leem, M. Cai Wang, P. Kang, SungWoo Nam, *Nano Lett.* **2015**, *15*, 7684.

(46) R. Goul, S. Das, Q. Liu, M. Xin, R. Lu, R. Hui, J. Z. Wu, *Carbon.* **2017**, *111*, 386.

(47) S. Xu, B. Man, S. Jiang, J. Wang, J. Wei, S. Xu, H. Liu, S. Gao, H. Liu, Z. Li, H. Li, H. Qiu, *ACS Appl. Mater. Interfaces.* **2015**, *7*, 10977.

(48) X. Li, X. Ren, Y. Zhang, W. C. H. Choy, B. Wei, *Nanoscale*. **2015**, *7*, 11291.

(49) H. Qiu, Y. Huo, Z. Li C. Zhang, P. Chen, S. Jiang, S. Xu, Y. Ma, S. Wang, H. Li, *ChemPhysChem*. **2015**, *16*, 2953.

(50) C. Yang, C. Zhang, Y. Huo, S. Jiang, H. Qiu, Y. Xu, X. Li , B. Man, *Carbon*. **2016**, 98, 526.

(51) H. Zhu, A. Liu, D. Li, Y. Zhang, X. Wang, W. Yang, J. Justin Gooding, J. Liu, *Chem. Commun.* **2017**, *53*, 3273.

(52) Y. Du, Y. Zhao, Y. Qu, Chia-Hao Chen, Chieh-Ming Chen, Cheng-Hao Chuange, Y. Zhu, *J. Mater. Chem. C*. **2014**, *2*, 4683.

(53) Y. Li, *MRS Communications.* **2018**, *8*, 79.

(54) Y Zhao, G. Chen, Y. Du, J. Xu, S. Wu, Y. Qu, Y. Zhu, *Nanoscale.* **2014**, *6*, 13754.

(55) L. Sun, H. Hu, D. Zhan, J. Yan, L. Liu, J. S. Teguh, E. K. L. Yeow, P. See Lee, Z. Shen, *Small*. **2014**, *10*, 1090.

(56) S. Nigara, Z. Zhou, H. Wang, M. Imtiaz, *RSC Adv.* **2017**, *7***,** 51546.

**Graphical Abstract:**